JOHANNES KEPLER
UNIVERSITY LINZ

SYNTHESIS AND CHARACTERISATION OF BISMUTH VANADATE PHOTOANODES FOR OXYGEN EVOLUTION REACTION

Submitted by
Dominik Böhm

Submitted at
Institute of Physical Chemistry and Linz Institute for Organic Solar Cells

Supervisor
o. Univ. Prof. Mag. Dr.DDr. h.c. Niyazi Serdar Sariciftci

Assistant Supervisor
DI Katarina Gugujonović

August 2022

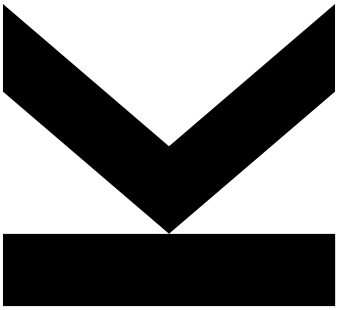

Bachelor Thesis
to confer the academic degree of
Bachelor of Science (BSc)
in the Bachelor's Program
Chemistry and Chemical Technology

JOHANNES KEPLER
UNIVERSITY LINZ

STATUTORY DECLARATION

I hereby declare that the thesis submitted is my own unaided work, that I have not used any sources other than those indicated and that all direct and indirect sources are acknowledged as references.

Place and Date

Signature

Abstract

Solar water splitting using photoelectrochemical approaches for the sustainable production of hydrogen has gained increasing interests over the last two decades. Amongst other inorganic compounds, bismuth vanadate is regarded one of the most promising photoanode materials for efficient solar water splitting. Bismuth vanadate bears the advantages of being an inexpensive, non-toxic and chemically stable *n*-type semiconductor. Compared with other photoanode compounds, bismuth vanadate possesses a more positive conduction band edge favourably near the hydrogen evolution potential allowing for water oxidation at comparably low externally applied bias.

This thesis aims at the synthesis and characterisation of bismuth vanadate photoanodes for a possible future implementation in photoelectrochemical tandem devices to promote the oxygen evolution reaction. The bismuth vanadate photoanodes were prepared according to a state-of-the-art two-step synthesis route. In the first step, a bismuth-containing precursor film was electrodeposited onto electrically conducting, transparent substrates. In the second step, after addition of a vanadium-containing precursor solution, the films were thermochemically transferred into bismuth vanadate photoanodes. It was found, that indigo exerts structure-ordering properties on the electrodeposition of the precursor film. During cyclic voltammetry, the prepared bismuth vanadate photoanodes already showed moderate photocurrents below the thermodynamic oxygen evolution potential of 1.23 V versus normal hydrogen electrode. However, compared with literature, the photoanodes showed only insufficient oxygen evolution rates and low Faraday efficiencies during photo-assisted electrolysis experiments. In further experiments, the topography as well as the optical properties of the photoanodes were investigated.

Exzerpt

Während der letzten beiden Jahrzehnte weckte die Möglichkeit der solaren Wasserspaltung mittels photoelektrochemischer Ansätze, zur nachhaltigen Produktion von Wasserstoff, weltweit zunehmendes Interesse unter Forschern. Bismutvanadat gilt neben anderen anorganischen Verbindungen als eines der vielversprechendsten Photoanodenmaterialien, das photokatalytische Wasserspaltung auch in großtechnisch effizientem Ausmaße ermöglichen soll. Bismutvanadat verbindet die Vorteile, ein kostengünstiger, ungiftiger und zugleich chemisch stabiler *n*-dotierter Halbleiter zu sein. Verglichen mit anderen potentiellen Photoanodenmaterialien, besitzt Bismutvanadat eine positivere Leitungsbandkante, die günstig nahe dem thermodynamischen Wasserstoffentwicklungspotential liegt, was eine Wasseroxidation bei vergleichsweise niedriger extern angelegter Vorspannung ermöglichen würde.

Das Ziel dieser Arbeit war die Synthese und Charakterisierung von Bismutvanadat-Photoanoden für eine mögliche zukünftige Implementierung in photoelektrochemischen Tandemzellen, wobei an ihnen die Sauerstoffevolutionsreaktion ablaufen soll. Die Bismutvanadat-Photoanoden wurden über einen, der Literatur bekannten, zweistufigen Syntheseweg hergestellt. Im ersten Schritt wurde ein bismuthaltiger Vorgängerfilm elektrolytisch auf elektrisch leitfähige, transparente Substrate abgeschieden. Im zweiten Schritt wurden die Filme nach Zugabe einer vanadiumhaltigen Vorgängerlösung thermochemisch in Bismutvanadat-Photoanoden umgewandelt. Es wurde festgestellt, dass Indigo strukturordnende Eigenschaften auf die elektrolytische Abscheidung des Vorgängerfilms ausübt. In den cyclovoltammetrischen Experimenten zeigten die Bismutvanadat-Photoanoden bereits mäßige Photoströme unterhalb des thermodynamischen Sauerstoffentwicklungspotentials von 1,23 V gegenüber der Normalwasserstoffelektrode. Im Vergleich zur Literatur zeigten die Photoanoden jedoch nur unzureichende Sauerstoffentwicklungsraten und niedrige Faraday-Effizienzen während der Photoelektrolysen. In weiteren Experimenten wurden die Topographie sowie die optischen Eigenschaften der Photoanoden untersucht.

Acknowledgements

First of all, I would like to express my sincerest thanks to o. Univ. Prof. Mag. Dr.DDr. h.c. Niyazi Serdar Sariciftci for giving me the opportunity to study and work on this thesis, which was of a rather unique topic for the Institute of Physical Chemistry and LIOS. Your lectures were always a great motivation for me to develop my interests in the field of physical chemistry.

Deepest gratitude is due to my supervisor DI Katarina Gugujonović, who always had an open ear for me answering upcoming questions with seemingly endless patience. I would like to take this opportunity to cordially thank you for your always motivating nature, the profound specialist knowledge you have made available to me, and the collegial as well as amicable cooperation.

Special thanks are also due to a. Univ. Prof. Dr. Markus Scharber, for the many fruitful discussions and his assistance with technical questions on optics and spectroscopy. I would like to express my gratitude to Dr. Dominik Wielend and DI Elisabeth Leeb for always helping me with questions regarding electrochemistry. Big thanks also to Nadine Kleinbruckner, BSc., for her assistance in electrochemistry and specially for introducing me into the preparation of Ag|AgCl quasireference electrodes. I would also like to thank Gabiele Hinterberger for her kind support on issues regarding technical equipment, especially gas chromatography.

Last but certainly not least, big thanks also to my family for supporting me through all the years and always showing strong interests in my studies.

Table of Contents

1. Introduction

Over the last 200 years, starting with the industrial revolution, technical and scientific inventions and discoveries brought mankind unprecedented prosperity as well as quality of life. The utilisation of fossil fuels and the electrification, which was promoted starting from the late 1880s, were largely responsible for these achievements [1, 2]. In 2020, more than 60 % of electricity worldwide was generated from fossil sources (coal, gas, oil) [3, 4]. With nearly 80 %, the share of fossil fuels on the worlds primary energy consumption was even higher [3, 5]. Although, for example, the forecast coal deposits would be sufficient for at least another century at current mining and consumption rates [6, 7], mankind must harness renewable energy sources in view of impending global warming.

Solar fuels would represent a possible alternative to fossil fuels. The expression “solar fuels” is an umbrella term for synthetic fuels produced by utilising solar energy [7, 8]. A prominent example for solar fuels is hydrogen, which could be produced by solar water splitting. An exemplary illustration of a water electrolysis cell for the production of hydrogen is given in **Figure 1 (a)**. The oxygen evolution reaction (OER) as well as the hydrogen evolution reaction (HER) would occur at an anode and cathode, respectively, which would be immersed in an electrolyte. The necessary bias of 1.23 V versus the normal hydrogen electrode (vs. NHE) needed to promote electrolysis (neglecting overpotentials and current losses) would be supplied by an external photovoltaic (PV) module. Therefore, this setup is usually referred to as photovoltaic-electrochemical (PV-EC) water electrolysis cell [9, 10]. A much more elegant method of producing hydrogen would be *via* water splitting using a so-called photoelectrochemical (PEC) tandem cell. Here, the word tandem refers to a stacked arrangement of certain photoresponsive layers [11]. The monolithic architecture of such PEC tandem cell would significantly reduce production costs and could reduce current losses compared to above-described PV-EC electrolysis units due to the absence of external wiring. However, durability and scalability are still major limitations preventing industrial PEC tandem cell applications [12]. Therefore, investigations and optimisations of different device architectures are currently the subject of research to overcome those limitations. A promising architecture, which also served as a motivation for this thesis, is shown in **Figure 1 (b)**. In this architecture, a bismuth vanadate ($BiVO_4$) photoanode would promote the OER on the illuminated frontside of the PEC tandem device. The HER would occur on the non-illuminated backside of the PEC tandem cell at a cathode. A solar cell within the tandem arrangement would provide the necessary bias to perform solar water splitting [13]. Major advantages of the PEC tandem device architecture shown in **Figure 1 (b)** result from the use of $BiVO_4$ as photoanode material. $BiVO_4$ is a very simple, inexpensive, non-toxic and chemically stable inorganic *n*-type semiconductor with a direct bandgap of 2.4 eV in the monoclinic scheelite

structure. Furthermore, $BiVO_4$ possesses a beneficial conduction band edge near the thermodynamic standard potential of the hydrogen evolution [14–16].

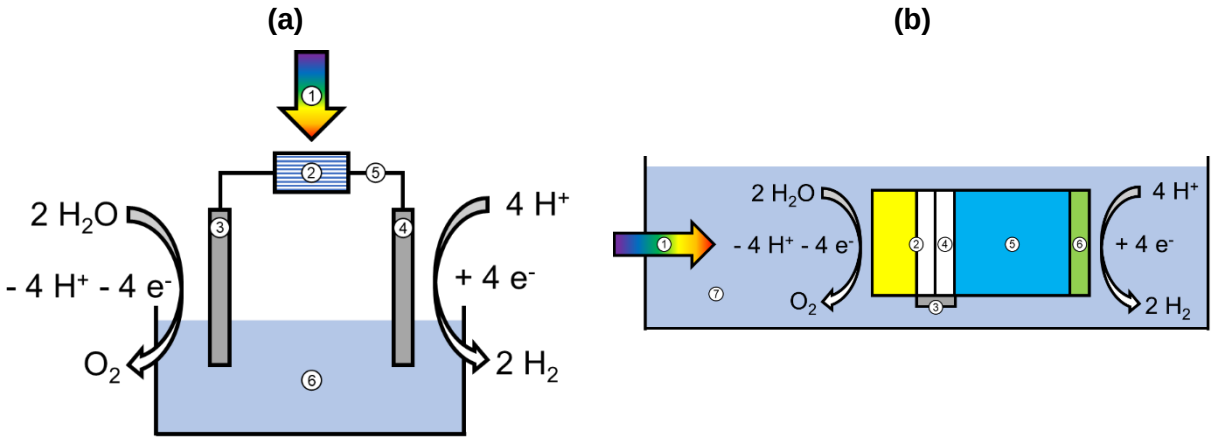

Figure 1: **(a)** Schematic illustration of a water electrolysis unit composed of separate electrodes, where (1) represents the incident sunlight which drives a (2) PV module supplying the necessary bias to perform the (3) OER and (4) HER on the anode and cathode, respectively. Both electrodes are immersed in an (6) aqueous electrolyte. The illustration was adapted and modified from [9] **(b)** Schematic illustration of a PEC tandem device. (1) represents the incident sunlight hitting the (2) $BiVO_4$ photoanode prepared on an electrically conducting, transparent substrate enabling the OER. A (3) silver contact allows for electrical connection with a (4) second electrically conducting, transparent substrate onto which a (5) solar cell is processed. (6) represents the cathode allowing for HER and (7) the aqueous electrolyte. The illustration was adapted and modified from [13].

The specific task of this bachelor thesis was the synthesis and characterisation of $BiVO_4$ photoanodes. The synthesis of such photoanodes was a novelty at the Institute of Physical Chemistry. The synthesised $BiVO_4$ photoanodes were characterised by means of profilometry, scanning electron microscopy (SEM), cyclic voltammetry (CV), UV-Vis spectroscopy, Fourier-transform infrared spectroscopy (FTIR) and external quantum efficiency (EQE). Additionally, photoassisted electrolysis experiments were performed where the produced amount of oxygen was quantified *via* gas chromatography (GC).

1.1. Physicochemical Working Principle of Photoelectrochemical Cells based on Semiconductor Electrodes

As mentioned, $BiVO_4$ is an inorganic *n*-type semiconductor. Contrary to a metal, in a semiconductor the valence and the conduction band are separated by a so-called bandgap with a defined bandgap energy (E_g). If a semiconductor absorbs light with an energy larger or equal to E_g, it may promote an electron from the valence into the conduction band. This creates mobile

charge carriers and makes the semiconductor conductive. If a semiconductor is immersed in an electrolyte, an electric field is formed at its surface due to charge transfer between the two phases. The direction of the electric field strongly depends on the doping of the semiconductor. In an *n*-type semiconductor, excess electrons fill parts of the conduction band whereby the electric field is formed from the semiconductor towards the electrolyte. If now light of an energy larger or equal E_g is absorbed by the semiconductor, an electron-hole pair is formed. However, due to the electric field present, the charges are immediately separated with the electron being driven towards the bulk of the semiconductor and the hole towards the semiconductor-electrolyte interface. In **Figure 2**, the presence of the electric field is represented by the bent valence and conduction band edges. Upon approaching the semiconductor-electrolyte interface, the hole may recombine with an electron from the oxide anion of a water molecule, promoting the OER at the photoanode. Note, that in order to promote this oxidation, the redox potential of the reactant must be energetically higher than the energy level of the hole at the interface. The electron may be used to promote the HER at the metal cathode. Note again, $BiVO_4$ possesses a very favourable conduction band edge near the thermodynamic standard potential of the hydrogen evolution. [17–20]

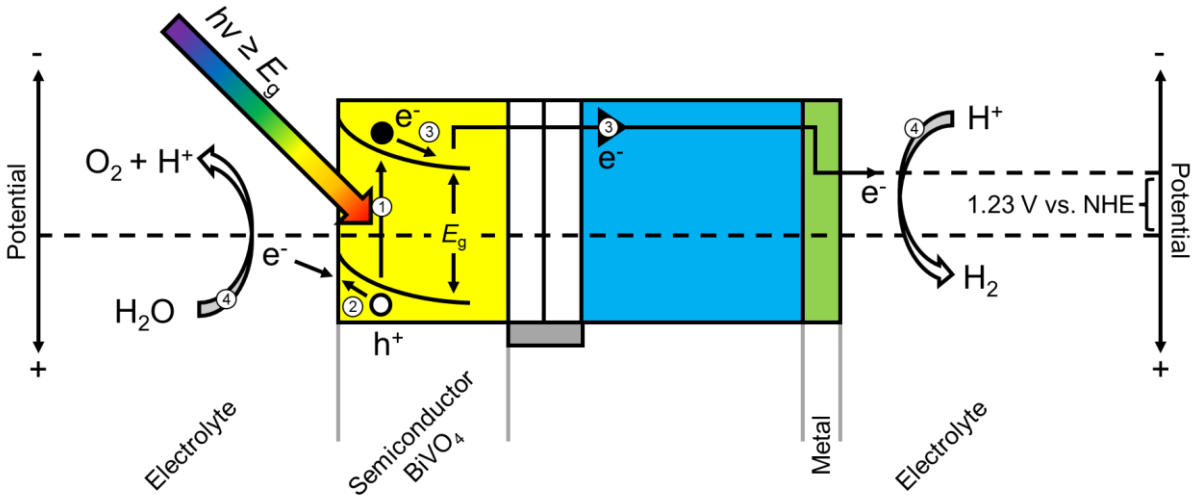

Figure 2: Schematic illustration of an energy diagram for a PEC tandem device composed of an *n*-type semiconductor $BiVO_4$ photoanode to promote the OER and a metal electrode to promote the HER. (1) represents the absorption of photons, (2) and (3) the separation of holes and electrons, respectively, due to the electric field and (4) the promoted electrochemical reactions. The illustration was adapted and modified from [20, 21].

1.2. Chemical Principles of the Synthesis of Bismuth Vanadate Photoanodes

Nowadays, it is state of the art to prepare $BiVO_4$ photoanodes *via* a two-step synthesis route. In the first synthesis step, a bismuth-containing precursor film is electrodeposited onto a suitable substrate. The precursor film is electrodeposited from an aqueous bismuth-containing electrolyte solution with the bismuth source being bismuth nitrate pentahydrate ($Bi(NO_3)_3{\cdot}5\ H_2O$), a white solid [13, 22]. The pH of the electrolyte must be acidic, because at neutral or basic pH values, bismuth(III) (Bi^{3+}) ions would precipitate as bismuth oxyhydroxide (BiOOH) according to **(1)**. However, even at acidic pH values, Bi^{3+} ions are instable in water and react to bismuth subnitrate ($BiONO_3{\cdot}H_2O$) according to **(2)** [23]. Therefore, Bi^{3+} ions have to be chemically stabilised by forming an inorganic complex. This may be achieved by dissolving an excess of sodium iodide (NaI) in the electrolyte solution. The iodide (I^-) ions stabilise the Bi^{3+} ions in the acidic aqueous solution by forming the tetraiodo bismuthate complex ($[BiI_4]^-$) according to **(3)** [22, 23]. Prior to electrodeposition, *p*-benzoquinone is added to electrolyte solution.

$$2\ Bi(NO_3)_3{\cdot}5\ H_2O + 6\ OH^- \rightarrow 2\ BiOOH_{(s)} + 6\ NO_3^- + 12\ H_2O \quad \textbf{(1)}$$

$$Bi(NO_3)_3{\cdot}5\ H_2O + H_3O^+ \rightarrow BiONO_3{\cdot}H_2O_{(s)} + 3\ H^+ + 2\ NO_3^- + 4\ H_2O \quad \textbf{(2)}$$

$$Bi(NO_3)_3{\cdot}5\ H_2O_{(s)} + 4\ NaI_{(aq)} \rightarrow Na[BiI_4]_{(aq)} + 3\ NaNO_{3\,(aq)} + 5\ H_2O \quad \textbf{(3)}$$

Electrodeposition is conducted chronoamperometrically using a standard three-electrode setup. During electrodeposition, two parallel reactions take place simultaneously, which ultimately lead to the formation of a bismuth-containing precursor film, composed of bismuth oxyiodide (BiOI), on the working electrode. Immediately after applying an appropriate potential between the working and the reference electrode, the electrochemical reduction of *p*-benzoquinone to hydroquinone is initiated according to **(4)**. In this reaction, protons (H^+) are consumed, increasing the local pH in the vicinity of the working electrode. This local increase of the pH triggers reaction **(5)**, leading to the precipitation of orange-brown BiOI onto the working electrode. The synthesis of BiOI films *via* this electrodeposition route bears the advantage of producing very thin two-dimensional BiOI crystals [22].

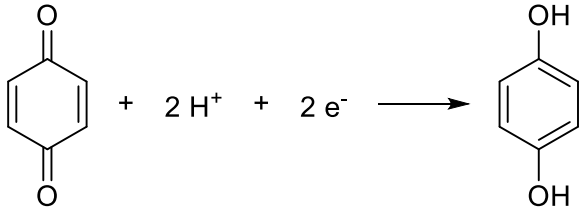

$E^0 = 0.70$ V vs. NHE **(4)**

$$Na[BiI_4]_{(aq)} + H_2O \rightarrow BiOI_{(s)} + 2\ H^+_{(aq)} + NaI_{(aq)} + 2\ I^-_{(aq)} \quad \textbf{(5)}$$

However, the electrodeposited BiOI films were found to be inhomogeneous, containing inclusions and defects. From metallurgy, certain organic additives are known which may positively influence electrowinning if admixed to the electrolysis bath. Most of the applied organic additives belong to the family of anionic surfactants. Examples are sodium mercaptopropane sulphonate and sodium lauryl sulphate, which are utilised for the electrowinning of copper [24] and nickel [25], respectively. Furthermore, additives specifically aimed at the electrodeposition of metal oxides are known. Organic dyes were reported to serve as effective additives for the preparation of zinc oxide photoanodes improving the homogeneity and smoothness of the deposited films [26]. Zinc oxide films are electrodeposited *via* a similar mechanism like the BiOI precursor films [27]. Therefore, it was evident to also investigate the influence of organic dyes, namely Eosin Y and indigo, on the electrodeposition of BiOI films. The chemical structures of the studied additives are shown in **Figure 3**.

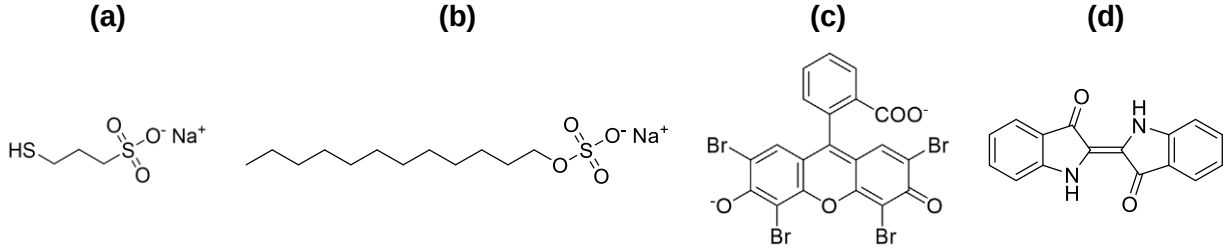

Figure 3: Chemical structures of the studied additives. **(a)** Sodium mercaptopropane sulphonate. **(b)** Sodium lauryl sulphate. **(c)** Eosin Y. **(d)** Indigo.

In the second synthesis step, the BiOI precursor films are thermochemically transformed into the photoactive $BiVO_4$ films. A solution of vanadyl acetylacetonate ($VO(acac)_2$) in dimethyl sulfoxide (DMSO) is drop-casted onto the BiOI precursor films. The substrates are placed in a tube furnace and subjected to a temperature program under oxidative conditions. It is important to increase the temperature of the oven at a small ramp rate to avoid the bismuth-containing film from peeling off the substrate [28]. The exact reaction mechanism occurring during the thermochemical transformation is still being discussed in literature. It is assumed, that in the first reaction stage iodine sublimes out of the BiOI precursor films yielding bismuth oxide (Bi_2O_3) and vanadium pentoxide (V_2O_5). In the second reaction stage, the formation of photoactive $BiVO_4$ may be caused by a solid-state reaction between Bi_2O_3 and V_2O_5. After the thermochemical transformation, excess brownish-black V_2O_5 crusts are dissolved in sodium hydroxide (NaOH) solution yielding pale yellow $BiVO_4$ photoanodes [13, 22].

2. Experimental

2.1. Chemicals and Materials

Table 1 summarises all chemicals and materials used to perform the experiments presented in this thesis. All chemicals and materials were used as described in **Table 1**, unless stated otherwise.

Table 1: Summary of the chemicals and materials used to perform the experiments presented in this thesis.

Chemical/Material	Abbreviation	Supplier	Purity / %
Ammomia water (0.1 M)	NH_4OH	---	---
Bismuth(III) nitrate pentahydrate	$Bi(NO_3)_3 \cdot 5\ H_2O$	Sigma-Aldrich	98
Boric acid	H_3BO_3	Alfa Aesar	99.99
Dimethyl sulfoxide	DMSO	VWR Chemicals	99.7
Eosin Y	---	Sigma-Aldrich	99
Fluorine doped tin oxide on glass (2.5 × 2.5 cm, 15 Ω sq^{-1})	FTO	Xin Yan Technology Limited	---
Hydrogen peroxide (30 wt-%)	H_2O_2	Merck	---
Indigo	---	---	---
Isopropanol	*i*-PrOH	VWR Chemicals	100.0
Nitric acid (65 wt-%)	HNO_3	VWR Chemicals	---
O_2 Test gas (5 Vol-% O_2 in N_2)	---	Linde	---
p-Benzoquinone	---	Sigma-Aldrich	98
Potassium ferrocyanide	$K_4[Fe(CN)_6]$	Merck	≥ 99
Potassium sulphate	K_2SO_4	Sigma-Aldrich	≥ 99.0
Sodium hydroxide	NaOH	Merck	p.a.
Sodium iodide	NaI	Sigma-Aldrich	≥ 99
Sodium lauryl sulphate	---	Sigma-Aldrich	≥ 99
Sodium mercaptopropane sulphonate	---	Sigma-Aldrich	90 (techn.)
Sulphuric acid (98 wt-%)	H_2SO_4	J.T. Baker	---
Toluene	---	VWR Chemicals	100.0
Vanadyl acetylacetonate	$VO(acac)_2$	Sigma-Aldrich	98

2.2. Synthesis of Bismuth Vanadate Photoanodes

The $BiVO_4$ photoanodes were prepared according to modified procedures reported in literature [13, 22]. All BiOI and $BiVO_4$ films were processed on glass substrates, coated with fluorine-doped tin oxide (FTO). These FTO substrates were prepared from 2.5 cm × 2.5 cm large substrates, as depicted in **Figure 4 (a)**. These substrates were cut in half centrally along the FTO coating using a glass cutter. The cutting direction is marked by a dashed line in **Figure 4 (b)**. An illustration of the resulting FTO substrates (≈1.2 cm × 2.5 cm), with which all further experiments were conducted, is given in **Figure 4 (c)**. The cut FTO substrates were cleaned with a toluene-soaked cotton cloth. The substrates were ultrasonicated in a cleaning solution prepared from 300 mL of deionised water and 10 mL of ammonia water (0.1 M) at 80 °C for 15 min. 2 mL of hydrogen peroxide were added to the cleaning solution and the substrates were ultrasonicated at 80 °C for further 15 min. Afterwards, the substrates were rinsed with deionised water for three times and ultrasonicated in isopropanol at 45 °C for 2 h. The cleaned substrates were dried with compressed air. Finally, an area of 0.25 cm^2 was defined on the FTO coating using a calliper and an adhesive tape as illustrated in **Figure 4 (d)**. All films were processed onto this 0.25 cm^2 large FTO area.

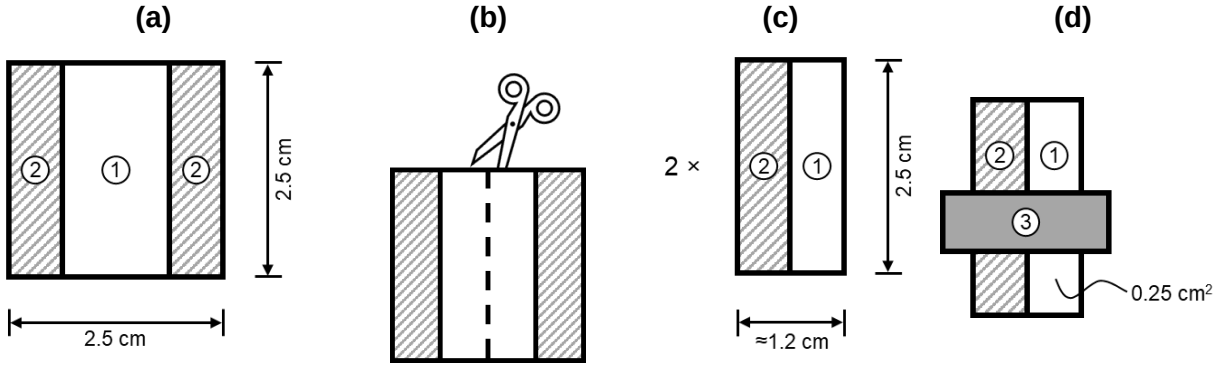

Figure 4: Schematic illustration of the preparation of the FTO substrates. **(a)** Precursor substrate, where (1) represents the FTO coating and (2) the underlying bare glass. **(b)** Cutting direction marked with a dashed line. **(c)** Resulting FTO substrate after cutting. **(d)** Defined area of 0.25 cm^2 on the FTO substrate, confined by an (3) adhesive tape.

As mentioned in the introduction, $BiVO_4$ films were prepared *via* a two-step synthesis route. In the first synthesis step, BiOI precursor films were electrodeposited onto FTO substrates. For the preparation of the required electrolyte solution, 1.199 g (8 mmol, 400 mM) of NaI were dissolved in 20 mL deionised water in a beaker under stirring. The pH of the colourless solution

was adjusted to 1.75 using nitric acid (HNO_3)[†]. Herein, 0.194 g (0.4 mmol, 20 mM) of $Bi(NO_3)_3 \cdot 5\ H_2O$ were dissolved to yield a deeply orange coloured solution. Larger crystals of $Bi(NO_3)_3 \cdot 5\ H_2O$ were crushed with a glass rod to shorten dissolution time. Next, 0.108 g (1 mmol, 50 mM) of *p*-benzoquinone were added to the solution. The pH of the resulting transparent, brown electrolyte was approximately 2.6. In a series of experiments, sodium mercaptopropane sulphonate, sodium lauryl sulphate, Eosin Y and indigo were added to the electrolyte solution to investigate their influence on the electrodeposition of the BiOI precursor films, as explained in chapter 1.2. The additive concentrations were varied between 1 and 30 mM. All other parameters remained unchanged. The electrolyte was ready to use directly after preparation.

For the electrodeposition of the BiOI precursor films, a standard three-electrode setup was used as depicted in **Figure 5 (a)**. The potentiostat was controlled *via* a computer interface. All electrodes were connected to the potentiostat using cables with crocodile clamps. The FTO substrates were connected as working electrode (WE) with the FTO coating facing plane-parallel towards a Pt counter electrode (CE) at a distance of 1 cm. A Ag|AgCl|3 M KCl reference electrode (RE) was placed 1 cm behind the WE. All electrodes were immersed in the previously prepared electrolyte. A top view of the electrode arrangement is given in **Figure 5 (b)**. Prior to electrodeposition, the RE was calibrated with potassium ferrocyanide. After arranging the three-electrode setup, the BiOI precursor films were electrodeposited chronoamperometrically by applying a potential of -100 mV vs. Ag|AgCl|3 M KCl for 5 min. For the deposition of BiOI films from the indigo containing electrolytes, a potential of -300 mV vs. Ag|AgCl|3 M KCl was applied for 5 min. The electrolyte was not stirred during electrodeposition. Thereupon, the adhesive tape was removed from the FTO substrates. Rinsing with deionised water and drying with compressed air yielded orange-brown BiOI precursor films adhering to the FTO substrates.

[†] In a series of experiments, it was found that the pH of the solution must be adjusted to a value between 1.50 and 2.00. Below a pH of 1.50, no films are formed in the subsequent electrodeposition step. Above pH values of 2.00, the deposited films appear exceedingly turbid.

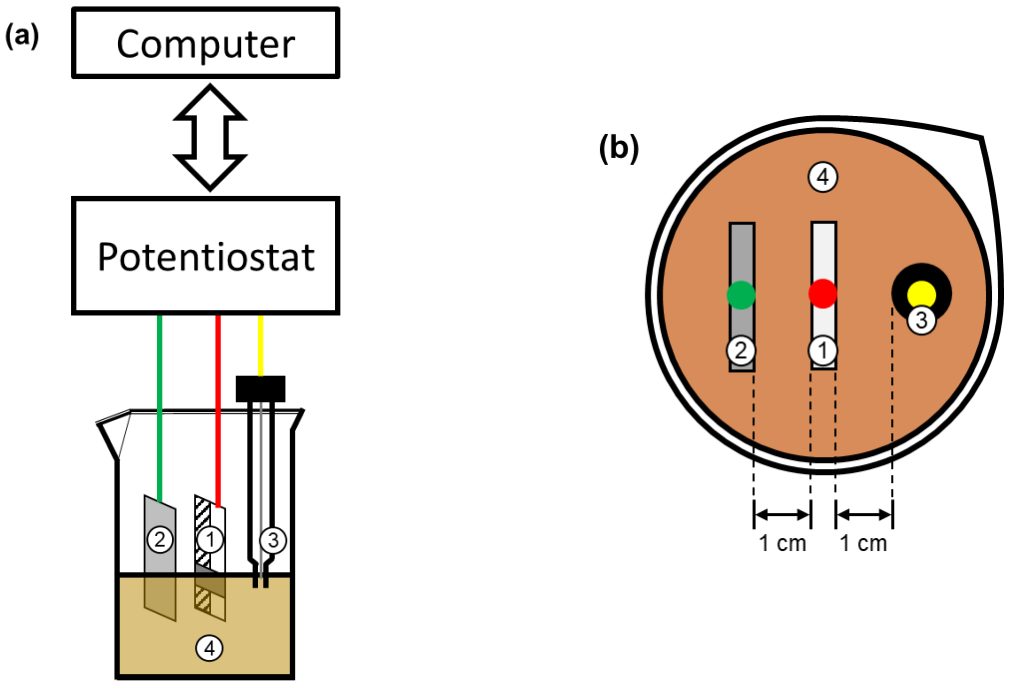

Figure 5: **(a)** Schematic illustration of the three-electrode setup used for the electrodeposition of the BiOI precursor films. (1) represents the WE (FTO substrate), which is immersed into the electrolyte until the electrolyte surface touches the adhesive tape, (2) the Pt CE, (3) the Ag|AgCl|3 M KCl RE and (4) the electrolyte. **(b)** Top view of the electrode arrangement.

In the second synthesis step, the BiOI precursor films were thermochemically transformed into the photoactive $BiVO_4$ films. Therefore, a vanadium-containing solution was prepared by dissolution of 0.530 g (2 mmol, 400 mM) $VO(acac)_2$ in 5 mL DMSO. 8.5 µL of this $VO(acac)_2$ solution were drop-casted onto the BiOI precursor films. The FTO substrates were placed inside a tube furnace with the still liquid drop-casted $VO(acac)_2$ solution on them. The tube furnace was heated from room temperature until a temperature of 450 °C at a ramp rate of 1 °C min^{-1}. The final temperature of 450 °C was held for 1 h. Then, the tube furnace was allowed to cool to room temperature again. Afterwards, the substrates were immersed in a 0.2 M NaOH solution for 20 min to dissolve the adhering black crust of V_2O_5. As a result, pristine pale yellow $BiVO_4$ films were obtained. These films were characterised by means of profilometry, SEM as well as UV-Vis and FT-IR spectroscopy. The $BiVO_4$ photoanodes used for CV and electrolysis experiments were modified by encapsulating the bare FTO above the $BiVO_4$ films with a microscope glass slide and epoxy resin. The epoxy resin was hardened with a UV lamp for 10 min.

2.3. Topographic Characterisations

2.3.1. Profilometry

The thickness of the pristine BiOI and $BiVO_4$ films was determined using a DekTak profilometer. A measurement force of 1 mg was applied at a scan rate of 100 µm s^{-1}. The measurements were conducted by moving the stylus from the probed surface towards the FTO coating. Every sample was probed for three times.

2.3.2. Scanning Electron Microscopy

The microscopic surface texture of the pristine BiOI and $BiVO_4$ films was analysed using SEM (JEOL JSM-6360LV) with a Bruker Nano X-Flash detector. The measurements were conducted at acceleration voltages of 7 kV.

2.4. Electrochemical Characterisations

All electrochemical characterisations were conducted in a special electrolysis cell, depicted in **Figure 6**. The electrodes were inserted into the electrolysis cell through two septa which were placed in the top lids. The encapsulated $BiVO_4$ photoanodes were connected as WE. An Ag|AgCl quasireference electrode was placed approximately 1 cm behind the WE. The quasireference electrode was calibrated using potassium ferrocyanide. A Pt electrode was used as CE. The anode and cathode compartment of the electrolysis cell were separated by a Nafion 117 membrane. All electrodes were connected to a potentiostat (Ivium V01218). The potential applied by the potentiostat between the WE and the RE was controlled *via* a computer interface. It was possible to illuminate the $BiVO_4$ photoanode through an optical window made of quartz glass. The photoanodes were illuminated with a Xe lamp (Müller Elektronik und Optik) with an irradiance of 45 to 55 mW cm^{-2}. The irradiance of the Xe lamp was estimated by illuminating a defined area of a calibrated Si solar radiation sensor (Mencke & Tegtmeyer GmbH) with the Xe lamp. The electrolysis cell was filled with a borate buffer. For its preparation, 3.09 g (50.0 mmol, 100 mM) of boric acid, 0.50 g (12.5 mmol, 25 mM) of NaOH and 8.71 g (50.0 mmol, 100 mM) of potassium sulphate were dissolved in 500 mL of deionised water under stirring. Finally, the pH of the buffer was adjusted to 8.50 using concentrated sulphuric acid.

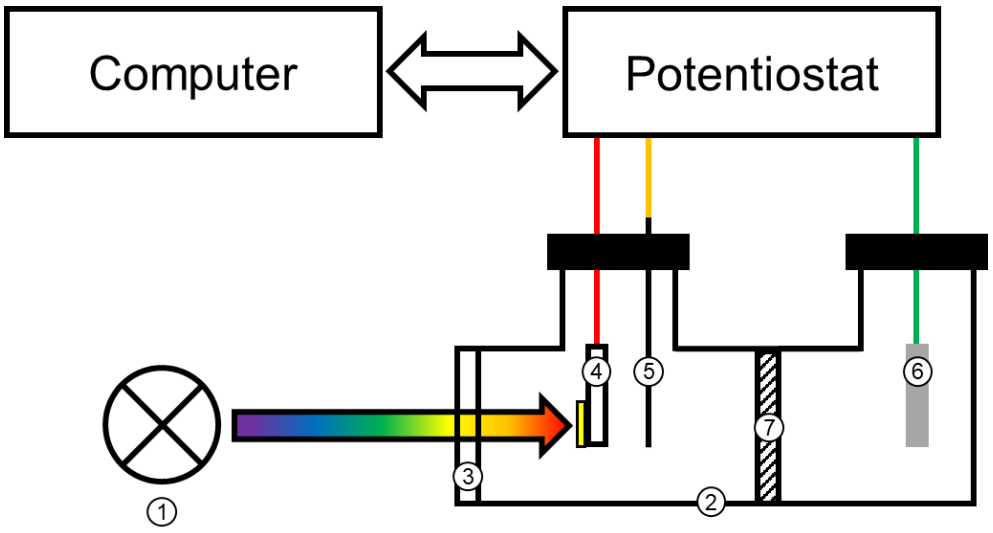

Figure 6: Schematic illustration of the setup used for electrochemical characterisations. (1) represents the Xe lamp, (2) the electrolysis cell filled with borate buffer (pH 8.50), (3) the optical window, (4) the $BiVO_4$ photoanode connected as WE, (5) the Ag|AgCl quasireference electrode, (6) the Pt CE and (7) the Nafion 117 membrane.

2.4.1. Cyclic Voltammetry

During every CV measurement, three full oxidative and reductive cycles were recorded at scan rates of 100 mV s^{-1}. Whilst some experiments, a Xe lamp (Müller Elektronik und Optik) was placed in front of the electrolysis cell, illuminating the $BiVO_4$ photoanode with an irradiance of 45 to 55 mW cm^{-2}. Some experiments were also conducted under chopped illumination by manually putting a piece of cardboard in the beam path at periodic intervals of 2 s.

2.4.2. Photoassisted Electrolysis Experiments and GC Quantification of evolved Oxygen

Prior to photoassisted electrolysis experiments, the anolyte was flushed with nitrogen for 10 min. The experiments were started, by applying a potential of 1.23 V vs. NHE between the WE and the RE. Throughout the whole experiments, the $BiVO_4$ photoanodes were illuminated with a Xe lamp (Müller Elektronik und Optik) at an irradiance of 45 to 55 W cm^{-2}. Quantification of the produced amounts of oxygen was conducted *via* GC. The quantifications were performed by manually injecting 2 mL gas sample from the gas space of the anode compartment into the gas chromatograph using a gas-tight syringe (VICI Pressure-Lok). The withdrawn gas volume in the gas space of the anode compartment was compensated by re-injecting 2 mL of pure nitrogen after sampling. The first sample was acquired before starting the experiments to be able to calculate the initial amount of oxygen present in the electrolysis cell. After starting the experiments, sampling was continued hourly. The experiments were conducted for at least four hours. Since the

electrolysis cell was not fully gas-tight, the oxygen drift from the atmosphere into the electrolysis cell was determined by prolonged sampling for further two to three hours after the experiments.

GC analyses were carried out using a Thermo Scientific Trace GC Ultra gas chromatograph equipped with an Agilent PorQ column. The injector was operated in the splitless mode. Nitrogen was used as a carrier gas at a constant flow rate of 20 mL min^{-1}. The oven temperature was maintained at 30 °C for the first 2 min of the analysis, then increased to 130 °C at a constant rate of 10 °C min^{-1} and finally kept at 130 °C for 8 min. A thermal conductivity detector operating at a temperature of 200 °C was used for detection. Oxygen was detected at a retention time of 0.3 min. Prior to GC quantification, a calibration curve was created using gas mixtures with known oxygen concentrations. These mixtures were prepared by injecting known volumes of a test gas containing 5 vol-% oxygen in nitrogen into a nitrogen-filled gas mouse. The resulting calibration curve is shown in **Figure 7**.

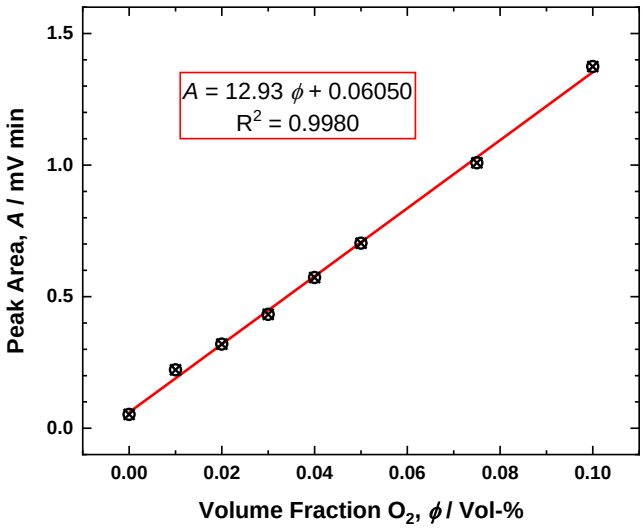

Figure 7: Calibration curve for oxygen quantification *via* GC.

As a result of the photoassisted electrolysis experiments, a diagram was obtained where the total amount of oxygen produced by the $BiVO_4$ photoanodes is plotted versus the respective electrolysis time. From this diagram it was possible to calculate the oxygen evolution rate of the photoanodes which was compared with literature values. Four important issues had to be considered for data evaluation. Firstly, as mentioned, 2 mL of the gas volume were taken during each sampling step and replaced with 2 mL nitrogen. The withdrawn sample volumes were non-negligible compared to the 31 mL of total gas volume in the gas space above the anolyte. The amounts of analyte (oxygen) in the withdrawn sample volumes accumulating over the entire measurement period influenced the results of every subsequent sampling step. Secondly, the entire evaluation is further complicated by the fact that new analyte is continuously being produced by the photoanodes. Thirdly, the measurement results had to be corrected for oxygen drift and

fourthly for the initially already present amount of oxygen. Data evaluation was conducted using **(6)**. This formula corrected the measurement results for sampling and at the same time accounted for the continuous oxygen evolution from the photoanodes. A theoretical derivation of this formula is presented in the appendix in chapter 5.1.

$$V_{O_2}(t_n) = V_{GC}(t_n) + 2\ \text{mL} \sum_{k=0}^{n-1} \varphi(t_k)\ ,\ \text{with n} > 0 \qquad \textbf{(6)}$$

In **(6)**, $V_{GC}(t_n)$ represents the volume of oxygen present in 31 mL of the total gas volume above the anolyte at the respective sampling time (t_n). $V_{GC}(t_n)$ has to be inserted with the unit mL. It may be calculated from the peak area obtained from GC measurements *via* the calibration curve, hence the index "GC". The correction for sampling is achieved with the summation term in **(6)**. This term adds up all the oxygen volumes withdrawn from the first sampling step (t_0) till the preceding sampling step (t_{n-1}). $\varphi(t_n)$ represents the volume fraction of oxygen at each sampling time. $\varphi(t_n)$ has to be inserted dimensionless. Therewith, $V_{O_2}(t_n)$, the volume of oxygen corrected for sampling and present in 31 mL of the total gas volume above the anolyte at the respective sampling time t_n, may be calculated. Then, the results had to be corrected for oxygen drift. This is exemplarily shown in **Figure 8**. There, $V_{O_2}(t_n)$ values are plotted versus the respective sampling times t_n. As can be seen in **Figure 8**, after the electrolysis was stopped only the oxygen drift was recorded indicated by a less steep incline in $V_{O_2}(t_n)$ than during electrolysis. The data points of the oxygen drift measurements may be approximated by a linear regression. Using the slope of this regression, the $V_{O_2}(t_n)$ values were corrected for oxygen drift. Finally, the data points were corrected for the initially already present oxygen volume. The oxygen volumes were converted into substance amounts using the ideal gas equation.

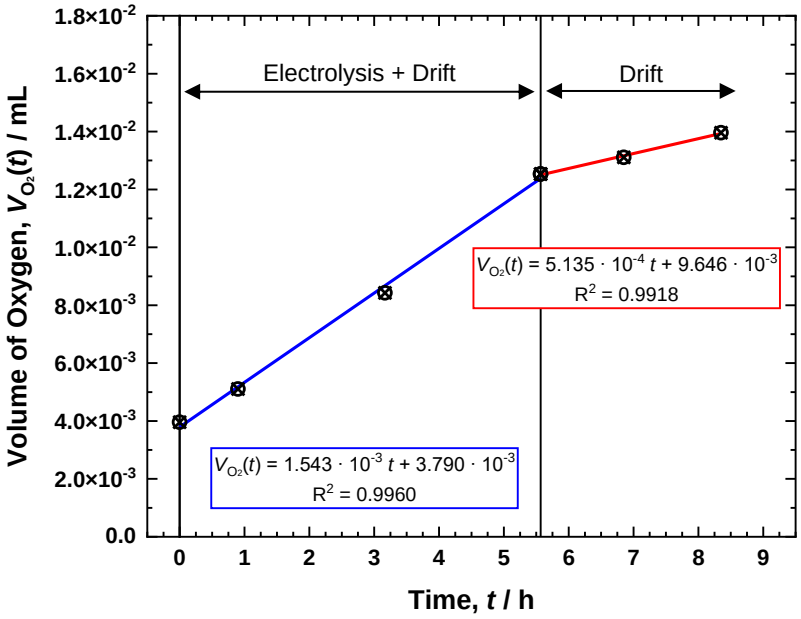

Figure 8: Exemplary graphical illustration of the correction of the oxygen volume for oxygen drift.

2.5. Spectroscopic Characterisations

2.5.1. UV-Vis Spectroscopy

For UV-Vis spectroscopy, very thin pristine BiOI and $BiVO_4$ films were prepared by shorten the electrodeposition time of the BiOI films to 20 s. The UV-Vis measurements were conducted with a double-beam UV-Vis-NIR spectrophotometer (Perkin Elmer UV-Vis-NIR Lambda 1050) equipped with an indium-gallium arsenide as well as a lead sulphide detector. The background correction was conducted with air only. The absorbance spectra of the BiOI and $BiVO_4$ films were recorded against FTO coated glass from 900 to 300 nm in 3 nm increments. Absorbance (*Abs*) was calculated from transmittance (*T*) according to IUPAC using **(7)** [29].

$$Abs = -\log_{10}(T) \qquad \textbf{(7)}$$

2.5.2. FTIR Spectroscopy

FTIR spectra were recorded from pristine BiOI and $BiVO_4$ films as well as indigo and *p*-benzoquinone powder samples with a Bruker Vertex 80 spectrometer in the attenuated total reflectance (ATR) mode. A liquid nitrogen-cooled mercury-cadmium telluride detector was used. The measurement chamber was flushed with nitrogen. The background correction was conducted with the nitrogen atmosphere inside the measurement chamber only. 100 scans were averaged per measurement.

2.5.3. External Quantum Efficiency

The setup used for EQE measurements is depicted in **Figure 9**. The light from a Xe lamp (LOT Quantum Design) was modulated by a chopper to a frequency of 17 Hz and passed through a monochromator (Oriel Instruments). The modulated and monochromatic light was focused through the optical window of the electrolysis cell, which was filled with a borate buffer (pH 8.50), onto the encapsulated $BiVO_4$ photoanode. The $BiVO_4$ photoanodes were connected as WE. An Ag|AgCl quasireference electrode was placed approximately 1 cm behind the WE. A Pt electrode was used as CE. The anode and cathode compartment of the electrolysis cell were separated by a Nafion 117 membrane. All electrodes were connected to a potentiostat (Jaissle, Model 1002 T-NC). During the measurements, a potential of 1.23 V vs. NHE was applied between the WE and the RE using the potentiostat. The detected current was amplified and converted into a voltage signal by a lock-in amplifier (Stanford Research Systems, Model SR 830 DSP), which operated at a frequency of 17 Hz. The signal was recorded by the computer which also controlled the monochromator. The setup was calibrated with a Si photodiode (Hamatsu S2281 1L019). The measurements were conducted from 300 to 550 nm in 10 nm increments.

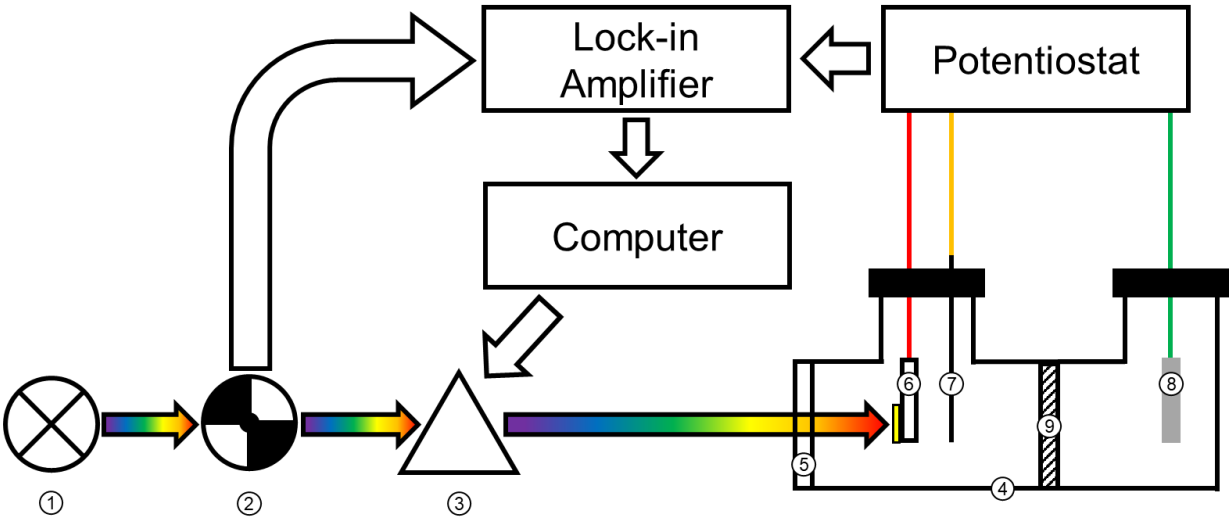

Figure 9: Schematic illustration of the EQE setup. (1) represents a Xe lamp, (2) a chopper, (3) a monochromator, (4) the electrolysis cell filled with borate buffer (pH 8.50), (5) the optical window, (6) the $BiVO_4$ photoanode connected as WE, (7) the Ag|AgCl quasireference electrode, (8) the Pt CE and (9) the Nafion mebrane.

The EQE at each excitation wavelength was calculated from the measurement results using **(8)**.

$$EQE(\lambda) = \frac{R_{\text{Photoanode}} \cdot S_{\text{Si}} \cdot h \cdot c}{R_{\text{Si}} \cdot \lambda \cdot e} \cdot 100\ \% \qquad \textbf{(8)}$$

In **(8)**, $R_{\text{Photoanode}}$ denotes the wavelength-dependent signal response of the photoanodes in mV, S_{Si} the wavelength-dependent sensitivity of the Si calibration cell in A W^{-1}, h the Planck constant ($6.626 \cdot 10^{-34}$ J s), c the speed of light ($2.998 \cdot 10^{8}$ m s^{-1}), R_{Si} the wavelength-dependent signal response of the Si calibration cell in mV, λ the wavelength of the incident light in m and e the elementary charge ($1.602 \cdot 10^{-19}$ C). S_{Si} values are tabulated in the appendix, R_{Si} values are obtained during calibration of the EQE setup and $R_{\text{Photoanode}}$ values are obtained as measurement results.

3. Results and Discussion

As outlined, the aim of this thesis was to synthesise and characterise $BiVO_4$ photoanodes for future implementation in PEC tandem devices to perform solar water splitting. However, the BiOI and $BiVO_4$ films synthesised according to [13, 22] were found to be inhomogeneous, containing inclusions and defects in the film structure. Thereupon, an attempt was started to improve the quality of both the BiOI precursor and the $BiVO_4$ films. As a starting point, the electrodeposition of the BiOI precursor films was optimised using organic additives, as explained in chapter 1.2. The use of sodium mercaptopropane sulphonate, sodium lauryl sulphate and Eosin Y showed no or hardly any improvements on the homogeneity of the resulting BiOI films. However, using indigo as an additive, it was possible to synthesise homogeneous BiOI films without any inclusions or defects for the first time. A concentration of 20 mM indigo in the electrolyte solution was found to yield the best results. At lower concentration, the BiOI films still contained few defects. Contrary, a higher indigo concentration showed no further improvements on the homogeneity of the electrodeposited BiOI films. Most likely, indigo was not included in the BiOI films, as can be seen from spectroscopic characterisations described in subsequent chapters. A possible explanation for the increased homogeneity of the BiOI films prepared with indigo may be derived from previous studies on the electrodeposition of zinc oxide. There, dye molecules were reported to form certain aggregates in the vicinity of the working electrode exhibiting structure directing properties on the growth behaviour of the zinc oxide films [26]. Similar mechanisms could also occur during the electrodeposition of BiOI films using indigo as an additive.

From profilometric measurements, the average thickness of the BiOI films prepared without and with indigo was determined to range from 470 to 510 nm and 420 to 450 nm, respectively, if they were electrodeposited at potentials of -100 mV vs. Ag|AgCl|3 M KCl. The average thickness of the BiOI films prepared with indigo could be adjusted to that of the BiOI films prepared without indigo, by applying a more negative potential of -300 mV vs. Ag|AgCl|3 M KCl during electrodeposition. Surprisingly, the more negative potential increased the homogeneity of the BiOI films even more. In **Figure 10 (a)**, orange-brown precursor films of BiOI prepared without and with indigo are depicted. Both BiOI films had a similar thickness. The direct comparison clearly shows the previously outlined increased homogeneity of the BiOI films prepared with indigo compared to the films prepared without indigo. Both, the BiOI films prepared with and without indigo showed a comparably smooth surface with a surface roughness of less than 20 nm. However, upon transformation of the BiOI films into the yellow $BiVO_4$ films, their surface roughness significantly increased to approximately 100 nm. This enhanced light scattering, whereby both, the $BiVO_4$ films prepared without and with indigo, appeared opaque as shown in **Figure 10 (b)**. Again, both $BiVO_4$ films prepared with and without indigo showed comparable thickness ranging from approximately 400 to 500 nm. Due to the rough surface of the $BiVO_4$ films, it was difficult to accurately measure the film thickness. Reasons for the increase of the surface roughness during thermochemical transformation of the BiOI films into the $BiVO_4$ films may be the possible evolution of gaseous iodine or the proposed solid reaction between bismuth oxide and vanadium pentoxide as outlined in chapter 1.2. As shown in **Figure 10 (b)**, the increased homogeneity of the BiOI films prepared with indigo did not affect the final appearance of the corresponding $BiVO_4$ films in comparison to the films prepared without indigo.

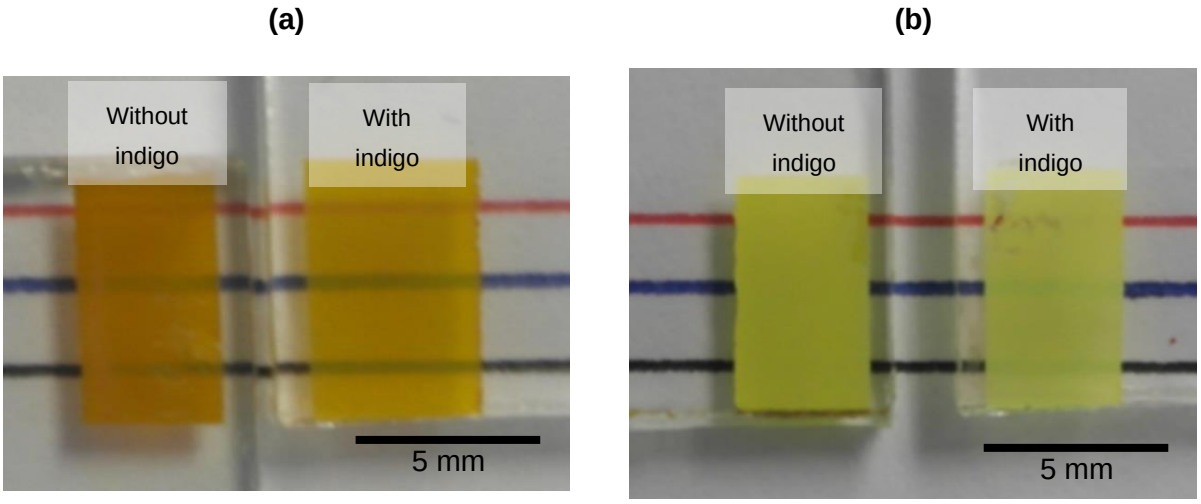

Figure 10: Photographs of the pristine **(a)** BiOI (film thicknesses of 470 to 510 nm) and **(b)** $BiVO_4$ films (film thicknesses of 400 to 500 nm) on FTO coated glass substrates. In each photograph, the left film was prepared without and the right film with indigo. The coloured lines in the background should enable a comparison of the different films.

Typical chronoamperogramms obtained during the electrodeposition of the BiOI precursor films are depicted in **Figure 11**. During the first few seconds of the electrodepositions, the chronoamperogramms showed an unexpected current density-time behaviour. Firstly, the current density decreased followed by an abrupt increase and finally decreased again exponentially. This behaviour was more pronounced during the electrodepositions without indigo. The further curve progression was nearly identical for the electrodepositions of the BiOI films prepared without and with indigo. The first decrease in current density may be due to the initiation of reaction **(4)**. During this reaction, *p*-benzoquinone and protons were consumed leading to a concentration gradient of both species in the vicinity of the WE. Due to the concentration gradient, the reaction rate would decrease until a dynamic equilibrium has been established between the reaction rate and the diffusion rate of educts from the bulk electrolyte towards the WE. However, initiation of reaction **(4)** ultimately triggered reaction **(5)**. During reaction **(5)**, protons were liberated again increasing the reaction rate of reaction **(4)**. Hence, the current density again increased shortly. The final exponential decrease in current density may be attributed to a few reasons. On the one hand, a dynamic equilibrium may have been formed between the reaction rates of reactions **(4)** and **(5)** as well as the diffusion rate of educts from the bulk towards the WE. On the other hand, during electrodeposition, the film thickness of the precipitated BiOI on the WE increased. Compared to FTO, BiOI is less conductive leading to a further decrease in current density.

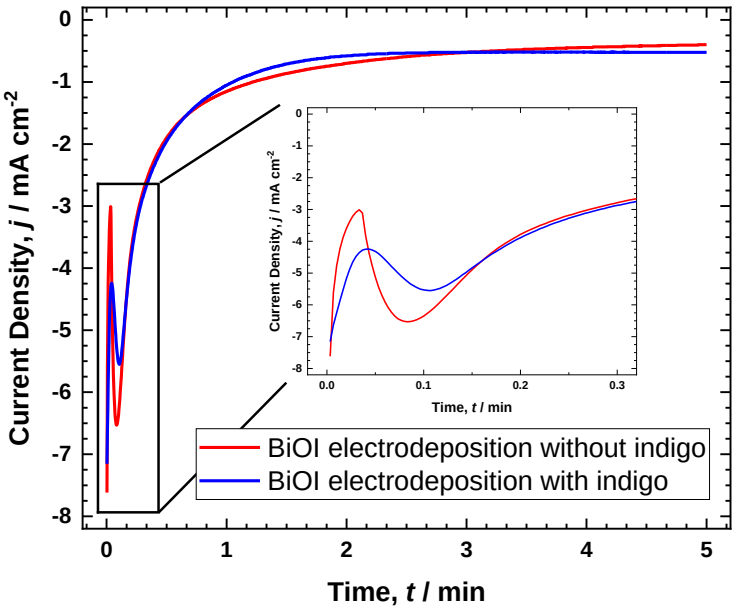

Figure 11: Chronoamperogramm obtained from BiOI electrodeposition.

In **Figure 12 (a) – (d)**, SEM images of the different BiOI and $BiVO_4$ films prepared without and with indigo are depicted. On a microscopic scale, the BiOI films showed a nanoworm morphology. Only slight differences in the crystal structure were observed between the BiOI films

prepared without (**Figure 12 (a)**) and with (**Figure 12 (b)**) indigo. The use of indigo yielded a slightly finer grain structure and a slightly denser grain packing. After thermochemical transformation, the resulting $BiVO_4$ films exhibited a nanoporous structure composed of spherical $BiVO_4$ agglomerates (**Figure 12 (c) and (d)**). The $BiVO_4$ films prepared with indigo showed a denser packing of the agglomerates and a more homogeneous distribution of the intervening pores. The observed nanomorphology of the BiOI and $BiVO_4$ films was in accordance with literature [22, 28, 30].

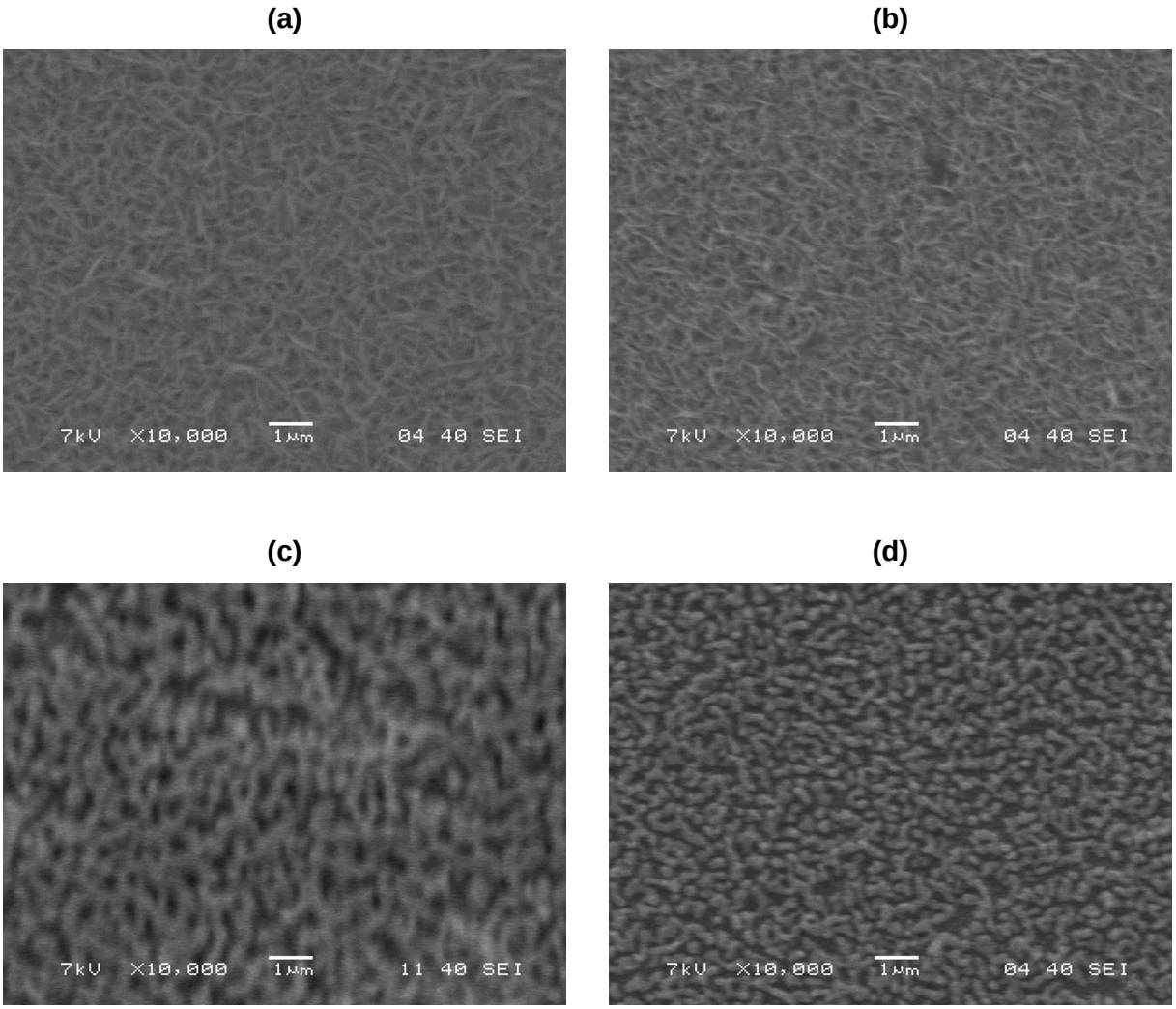

Figure 12: SEM images of pristine **(a)** BiOI film prepared without indigo, **(b)** BiOI film prepared with indigo, **(c)** $BiVO_4$ film prepared without indigo and **(d)** $BiVO_4$ film prepared with indigo.

3.1. Spectroscopic Characterisations

3.1.1. UV-Vis Spectroscopy

Figure 13 shows the UV-Vis spectra of BiOI and $BiVO_4$ films prepared with and without indigo. The spectra were recorded from BiOI and $BiVO_4$ films with thicknesses of 280 to 300 nm and 200 to 300 nm, respectively. All BiOI and $BiVO_4$ films showed strong absorption in the UV and visible violet-blue colour range, between 300 and 500 nm and a pronounced decrease in absorbance below 300 nm. Above 500 nm, the absorbance all BiOI films and the $BiVO_4$ film prepared without indigo decreased, whereas the $BiVO_4$ film prepared with indigo shows another absorption band. The UV-Vis spectra of the BiOI and $BiVO_4$ films prepared without indigo were in accordance with literature [14]. It is questionable, whether the additional band around 570 nm of the $BiVO_4$ film prepared with indigo originated from the absorption of indigo included in the film. There are many indications that this band does not originate from the absorption of indigo included in the film. The band may be rather attributed to light scattering on the $BiVO_4$ films. First of all, it should be remembered that the $BiVO_4$ films were very rough (surface roughness of approximately 100 nm). In general, rough films strongly promote light scattering [31]. Furthermore, a pure indigo thin film would show an absorption maximum at 650 nm [32] and not at 570 nm. Then, If the band around 570 nm would originate from light absorption, the $BiVO_4$ film would appear black because it would absorb light from almost the entire visible light spectrum. Conversely, the $BiVO_4$ films had a pale-yellow colour. If indigo was included in the $BiVO_4$ film, it could only originate from the BiOI precursor films. Therefore, also the BiOI films prepared with indigo should show the supposed absorption band at around 570 nm. However, the BiOI films do not show any indication of an absorption band around 570 nm. Furthermore, if indigo would have already been included in the BiOI precursor films, it would have also undergone the thermochemical treatment at 450 °C. Since indigo already sublimes at 300 °C and decomposes above 390 °C [33], it would be highly unlikely that indigo would be still included in the resulting $BiVO_4$ films. The FTIR and EQE measurements explained in subsequent chapters provide further evidence that indigo was probably not contained in the $BiVO_4$ films.

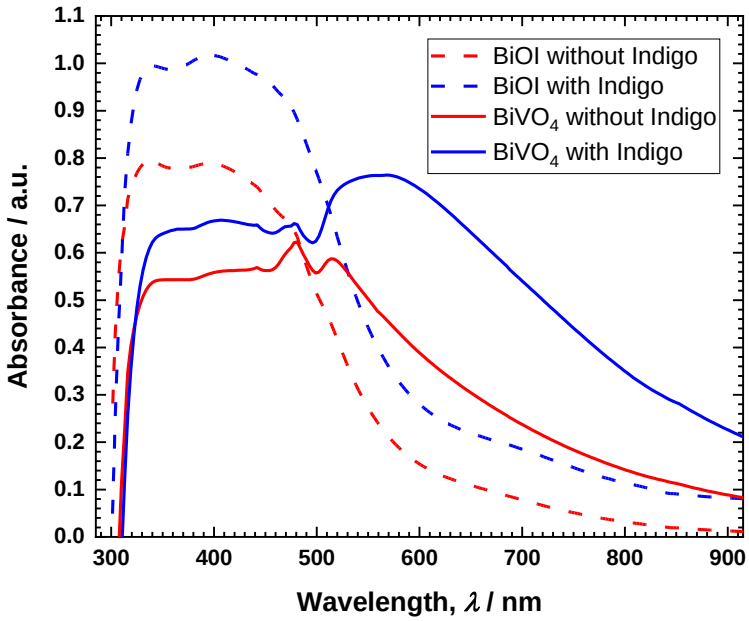

Figure 13: UV-Vis spectra of BiOI and $BiVO_4$ films on FTO coated glass prepared with and without indigo.

3.1.2. FTIR Spectroscopy

The FTIR spectra recorded from the BiOI and $BiVO_4$ films as well as indigo and *p*-benzoquinone powders are depicted in **Figure 14**. It was not possible to correct the BiOI and $BiVO_4$ spectra for the FTO background signal due to different penetration depths of the IR radiation during the measurements. Therefore, the FTIR spectrum of the pure FTO coating on glass is also shown in **Figure 14**. Comparing the spectra of the BiOI and $BiVO_4$ films with the spectrum of FTO indicates that the majority of the measured signals from the films originate from the FTO background. Only the $BiVO_4$ films showed an additional signal between 950 and 600 cm^{-1} not originating from the FTO background. This signal may be related to the bending vibration of the vanadate anion [34]. The FTIR spectra revealed no evidence that the BiOI and $BiVO_4$ films prepared with indigo contained any indigo. On the one hand, the $BiVO_4$ films prepared with and without indigo do not show any differences between their spectra. The same argument applies to the BiOI precursor films. On the other hand, the BiOI and $BiVO_4$ spectra of the films prepared with indigo do not match the spectrum of pure indigo at all. Finally, a comparison of the spectra of the BiO and $BiVO_4$ films with that of *p*-benzoquinone shows that most likely no *p*-benzoquinone was included in the films either.

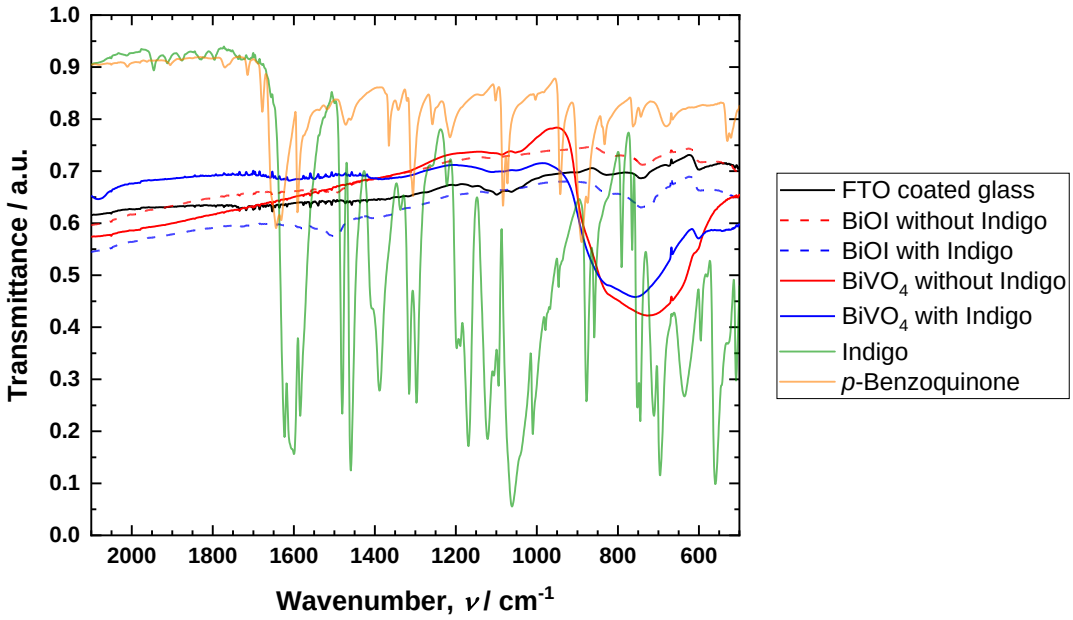

Figure 14: FTIR spectra of BiOI and $BiVO_4$ films on FTO coated glass prepared with and without indigo as well as FTIR spectra of indigo and *p*-benzoquinone powder samples.

3.1.3. External Quantum Efficiency

The EQE spectra of the $BiVO_4$ photoanodes are depicted in **Figure 15**. Between 350 and 470 nm, both photoanodes prepared with and without indigo showed moderate EQE of approximately 30 and 25 %, respectively. The EQE spectra were in accordance with literature [13]. The recorded data might be subjected to small errors, since the calibration of the EQE setup with the Si cell was conducted in a different optical medium (air) than the actual EQE measurements (aqueous borate buffer). It was not possible to record any EQE signal below 350 nm, because the Si cell used for calibration did not respond in this wavelength range. Between 470 and 500 nm, the EQE of both $BiVO_4$ photoanodes abruptly decreased to 0 %. This is a further indication that the band around 570 nm in the UV-Vis spectrum of the $BiVO_4$ film prepared with indigo may originate from light scattering and not from light absorption.

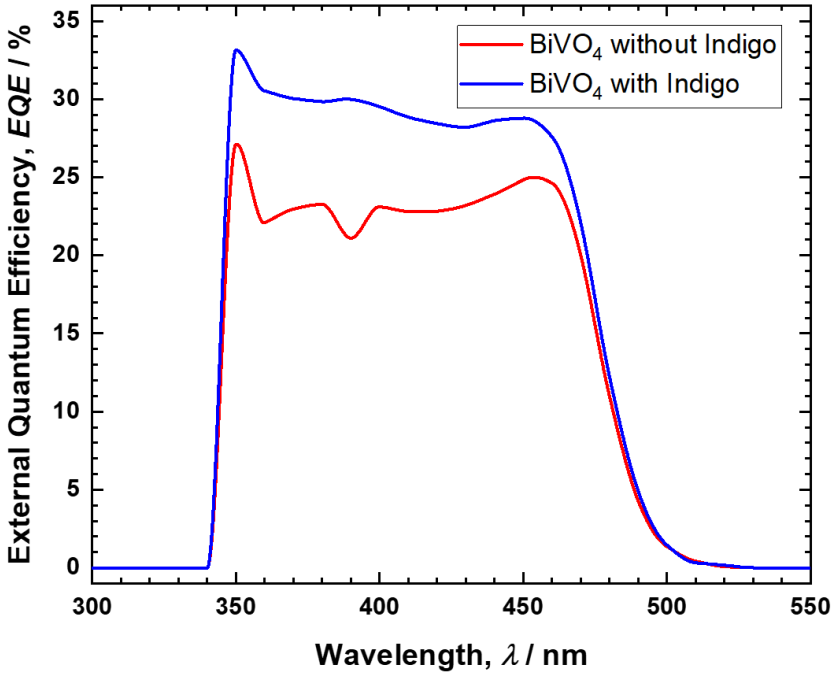

Figure 15: EQE spectra of $BiVO_4$ photoanodes prepared with and without indigo, recorded at a potential of 1.23 V vs. NHE in a borate buffer (pH 8.5).

3.2. Electrochemical Characterisations

3.2.1. Cyclic Voltammetry

Figure 16 (a) shows the cyclovoltagramms of $BiVO_4$ photoanodes prepared with and without indigo. For the non-illuminated photoanodes, photocurrents were only measured above potentials of approximately 1.5 V vs. NHE. Contrary, upon illumination photocurrents were detected even at potentials below 1.23 V vs. NHE. This comparison confirms the photoelectrocatalytic effect of the $BiVO_4$ photoanodes upon illumination. The photoanodes effectively promote the OER in the potential range around 1.23 V vs. NHE. Regardless of illumination, the photoanodes prepared with indigo always showed larger photocurrents above potentials of 1.0 V vs. NHE than the photoanodes prepared without indigo. The local decrease in photocurrents between 1.8 and 2.0 V vs. NHE can be attributed to the slow mass transport kinetics of ionic species in the borate buffer [13]. The cyclovoltagramms do not show reductive peaks, since the oxygen evolved during the oxidative CV scans separated as a gas from the WE. For a better illustration of the photoelectrocatalytic effect of the photoanodes on the OER, some cyclicovoltagramms were recorded under chopped illumination. **Figure 16 (a)** and **(b)** depict the cyclovoltagramms recorded under chopped illumination for $BiVO_4$ photoanodes prepared without and with indigo, respectively. The figures clearly show, that upon interrupting illumination, the current densities abruptly dropped to the level which was recorded without illumination for both

photoanodes. When the photoanodes were illuminated again, the photocurrents increased to approximately the level recorded under continuous illumination. For a sake of clarity, only the measurement results obtained from oxidative scanning directions are depicted.

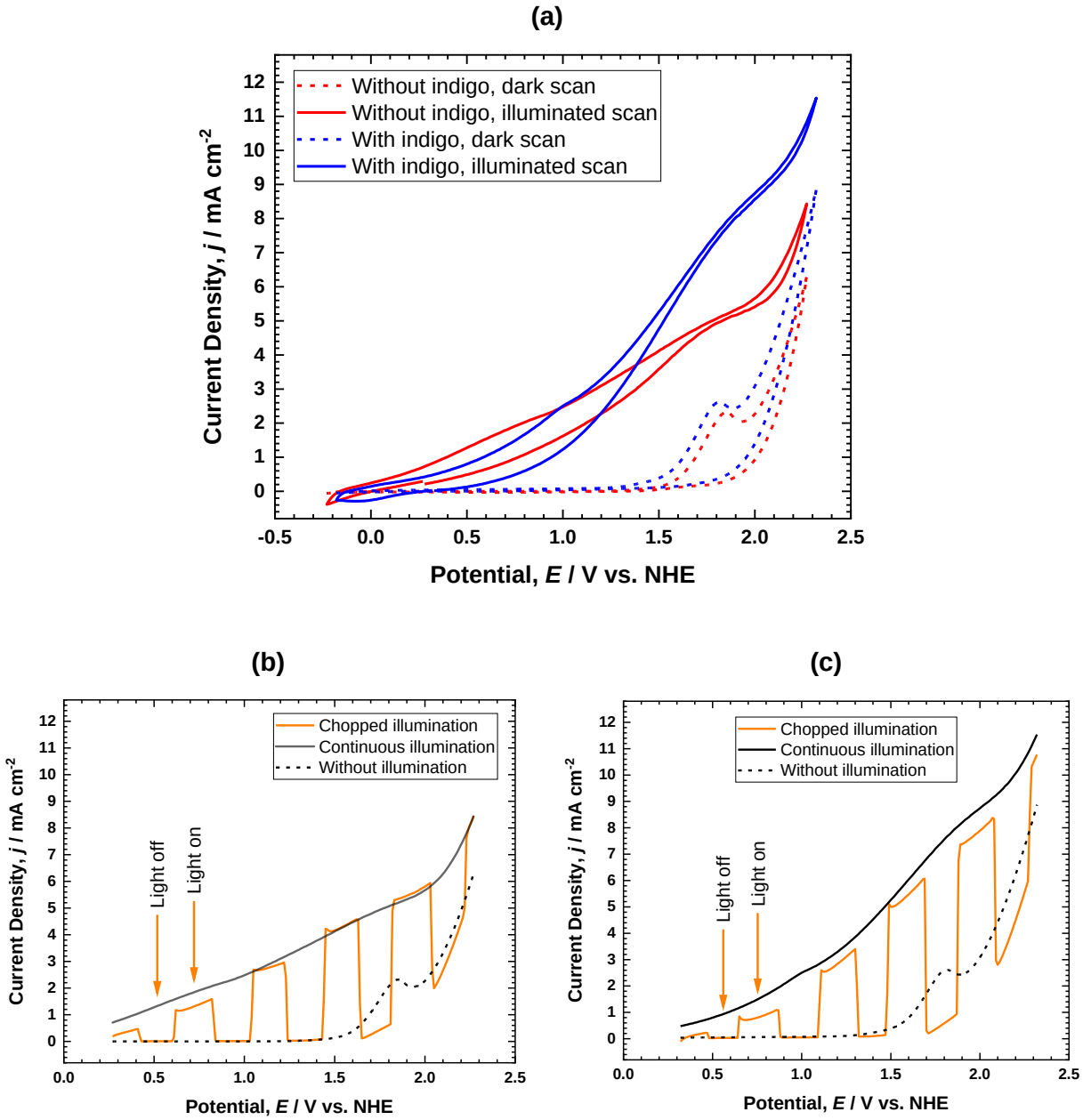

Figure 16: Cyclovoltagramms of $BiVO_4$ photoanodes recorded in borate buffer (pH 8.5) at scan rates of 100 mV s^{-1}. **(a)** Comparison of $BiVO_4$ photoanodes prepared with and without indigo in the dark and under continuous illumination with a Xe lamp (irradiance of 50 mW cm^{-2}). **(b)** Influence of chopped illumination on oxidative CV scan of $BiVO_4$ photoanode prepared without indigo. **(c)** Influence of chopped illumination on oxidative CV scan of $BiVO_4$ photoanode prepared with indigo.

3.2.2. Photoassisted Electrolysis Experiments and GC Quantification of evolved Oxygen

From the photoassisted electrolysis experiments, the oxygen evolution rates of the $BiVO_4$ photoanodes were calculated. All results were normed to the electrode surface and corrected for oxygen background leakage. Three measurements each were performed for the photoanodes prepared without and with indigo, the results of which are summarised in **Table 2**. The photoanodes prepared without and with indigo showed comparable oxygen evolution rates of approximately 180 nmol cm^{-2} h^{-1}. From **Figure 16 (a)** it may be seen, that the photoanodes prepared without and with indigo showed similar current densities at a potential of 1.23 V vs. NHE. Therefore, it seems plausible that both types of photoanodes also showed similar oxygen evolution rates at this potential. One reason for the noticeable range of variation of the results listed in **Table 2** could be possible fluctuations in the emitted irradiance of the Xe lamp used to illuminate the photoanodes. Furthermore, the incidence angle of the light shone from the Xe lamp onto the photoanodes could have varied between the different measurements. Further possible explanations may be deviations due to errors made during sampling, oxygen leakages into the syringe whilst sample transfer or oxygen leakages into the gas chromatograph, especially since the detected amounts of oxygen are very small compared to the abundant amounts of oxygen in the atmosphere. If the deviations are due to leakages of oxygen from the atmosphere other than the oxygen drifts, they seem acceptable considering that the oxygen content in the atmosphere is around 100 times higher than the detected oxygen concentrations.

Table 2: Summary of the oxygen evolution rates obtained from the photoassisted electrolysis experiments of the $BiVO_4$ photoanodes prepared with and without indigo at potentials of 1.23 V vs. NHE.

Measurement number	Oxygen evolution rate of $BiVO_4$ photoanode prepared without indigo / nmol cm^{-2} h^{-1}	Oxygen evolution rate of $BiVO_4$ photoanode prepared with indigo / nmol cm^{-2} h^{-1}
1	195	187
2	174	191
3	182	170
Arithmetic mean	184	183

Figure 17 (a) and **(b)** show exemplary illustrations of the time course of some measured and calculated parameters during the electrolysis experiments of the $BiVO_4$ photoanodes prepared without and with indigo, respectively. The black curves represent the chronoamperometric current density traces. After an initial decrease, the current densities levelled

at approximately 1.2 to 1.4 mA cm^{-2} for both types of photoanodes. The orange curves indicate a linear increase of the produced substance amount of oxygen throughout the experiments. The orange circles indicate the sampling times. The time courses of the calculated Faraday efficiencies are illustrated with green curves. Only very small Faraday efficiencies of about 0.5 to 1.3 % were achieved. The low oxygen evolution rates as well as low Faraday efficiencies may be attributed to the very poor electron-hole separation yields in $BiVO_4$ films [16, 30].

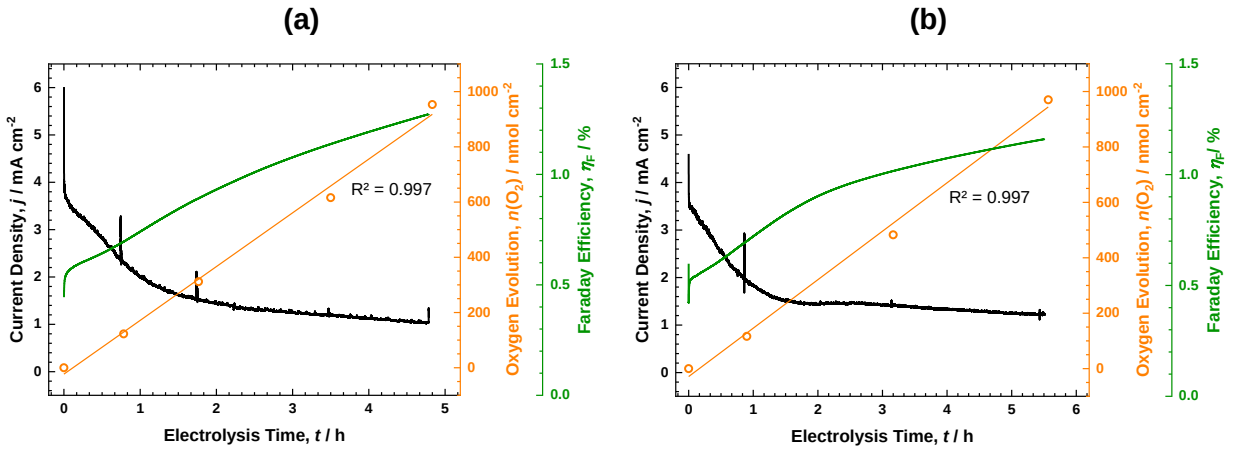

Figure 17: Exemplary chronoamperometric traces of oxygen evolution current density, evolved substance amount of oxygen and oxygen Faraday efficiency of $BiVO_4$ photoanodes prepared **(a)** without and **(b)** with indigo.

4. Conclusion and Outlook

During this thesis, it was possible to successfully synthesise $BiVO_4$ photoanodes for a potential implementation in future PEC tandem devices. It was demonstrated that indigo positively influences the electrodeposition of BiOI precursor films by increasing their homogeneity compared to BiOI films prepared without indigo. Unfortunately, the increased homogeneity of the BiOI films showed no influence on the final appearance of the $BiVO_4$ photoanodes. However, the $BiVO_4$ photoanodes prepared with indigo achieved higher current densities above potentials of 1.2 V vs. NHE during CV and about 5 % higher EQE values than the photoanodes prepared without indigo. As shown in a series of experiments, these differences in CV as well as EQE measurements may most likely not be attributed to residual indigo included in the $BiVO_4$ films. It may be rather assumed, that during the electrodeposition of BiOI, indigo positively influences the microstructure of the deposited film. Subsequently, these changes may also affect the $BiVO_4$ films which thereupon show better CV and EQE results. Indeed, minor differences in the microstructure of the BiOI and $BiVO_4$ films prepared with and without indigo could be determined during the SEM measurements. During the photoassisted electrolysis experiments, both, the $BiVO_4$ photoanodes prepared without and with indigo, showed similar oxygen evolution rates and Faraday efficiencies.

For a future implementation of the $BiVO_4$ photoanodes in PEC tandem devices, certain properties of the $BiVO_4$ photoanodes would still need to be improved. On the one hand, both, the oxygen evolution rate as well as the Faraday efficiency of the photoanodes, have to be increased. This may be achieved by the implementation of a co-catalyst system on the $BiVO_4$ films. Nowadays, numerous co-catalyst systems are reported in literature [30, 35]. Another strategy reported in literature would be to dope the $BiVO_4$ films with certain transition metal ions [16, 36]. On the other hand, the transparency of the $BiVO_4$ films has to be optimised by reducing their surface roughness to decrease light scattering. This issue is important, because the $BiVO_4$ photoanodes represent the very first photoactive layer in the potential PEC device as shown in **Figure 1 (b)**. If the photoanodes would be utilised in their current conformation, a considerable part of the light spectrum would already be lost due to light scattering at the photoanodes and would not be passed to further photoactive layers. As shown in this thesis, it is difficult to optimise the optical properties of the $BiVO_4$ films *via* the applied two-stage synthesis route. The surface roughness always increased considerably during the thermochemical conversion in the second synthesis step, independently of the homogeneity of the BiOI precursor films. This problem may be circumvented if the synthesis route were reduced to a single electrochemical step to be able to exert a direct influence on the surface roughness of the formed $BiVO_4$ films. Currently, only few literature was published on one-step $BiVO_4$ photoanodes synthesis. To the best of the authors knowledge, no literature at all was published on an electrochemical one-step synthesis route. Only pyrochemical one-step synthesis routes are reported [37]. A possible reaction equation for a future electrochemical one-step synthesis route is given in **(9)**. There, $Bi(NO_3)_3$ and sodium metavanadate ($NaVO_3$) would directly react to $BiVO_4$. This reaction would utilise the same electrodeposition mechanism as presented for BiOI in this thesis. Again, a local pH increase in the vicinity of the WE of an electrochemical three-electrode setup would trigger the precipitation of $BiVO_4$. However, a method would have to be found to stabilize Bi^{3+} ions in the aqueous precursor electrolyte solution to prevent the formation of $BiONO_3 \cdot H_2O$ as shown in **(2)**.

$$Bi(NO_3)_{3\,(aq)} + NaVO_{3\,(aq)} + H_2O \rightarrow BiVO_{4\,(s)} + NaNO_{3\,(aq)} + 2\,H^+ + 2\,NO_3^- \qquad \textbf{(9)}$$

5. Appendix

5.1. Theoretical Derivation of Equation (6)

As outlined in chapter 2.4.2. the measurement results had to be corrected for sampling using equation **(6)**. In this chapter, equation **(6)** should be theoretically derived. At time zero of the electrolysis (t_0) only the base amount of oxygen ($V_{O_2}(t_0)$) is present in the gas space above the anolyte. $V_{O_2}(t_0)$ may be quantified *via* GC from 2 mL sample of the gas space. The sampled volume is replaced with 2 mL nitrogen. $V_{O_2}(t_0)$ may be calculated from the volume fraction of

oxygen at t_0 ($\varphi(t_0)$) which is calculated from the oxygen peak area of the gas chromatogram using the calibration line:

$$V_{O_2}(t_0) = 31\ \text{mL} \cdot \varphi(t_0)\ ,\ \text{the gas space above the anolyte has a volume of 31 mL} \quad \textbf{(10)}$$

Directly after sampling, the electrolysis is started. Assume, sampling is conducted again in one hour (t_1). During the next hour, a certain amount of oxygen accumulates due to oxygen evolution at the photoanodes and due to oxygen drift ($V_{O_2,acc}(t_0 \rightarrow t_1)$). If sampling is conducted at t_1 (again the sampled volume is replaced with pure nitrogen to keep the total gas space volume costant), $\varphi(t_1)$ may be calculated from the oxygen peak area of the gas chromatogram. However, inserting $\varphi(t_1)$ into **(10)** would not yield the total amount of oxygen present at t_1. Remember, that 2 mL sample were removed from the gas space during sampling at t_0. If $\varphi(t_1)$ was inserted into **(10)**, only an auxiliary quantity ($V_{GC}(t_1)$) would be obtained (the index "GC" should indicate, that this quantity is the oxygen amount directly obtained from GC). $V_{GC}(t_1)$ would be composed of the following oxygen quantities:

$$V_{GC}(t_1) = V_{O_2}(t_0) - 2\ \text{mL}\ \varphi(t_0) + V_{O_2,acc}(t_0 \rightarrow t_1) \quad \textbf{(11)}$$

Therefore, $V_{O_2}(t_1)$ has to be calculated from $V_{GC}(t_1)$ by correcting it for sampling during t_0:

$$V_{O_2}(t_1) = V_{GC}(t_1) + 2\ \text{mL}\ \varphi(t_0) \quad \textbf{(12)}$$

The previous derivation may be verified by inserting **(11)** for $V_{GC}(t_1)$ in **(12)**:

$$V_{O_2}(t_1) = V_{O_2}(t_0) - 2\ \text{mL}\ \varphi(t_0) + V_{O_2,acc}(t_0 \rightarrow t_1) + 2\ \text{mL}\ \varphi(t_0) = \quad \textbf{(13)}$$
$$= V_{O_2}(t_0) + V_{O_2,acc}(t_0 \rightarrow t_1)$$

Analogously, $V_{O_2}(t_2)$ may be derived. Assume once more, sampling is conducted in one hour (t_2). During the next hour, again a certain amount of oxygen will accumulate due to oxygen evolution at the photoanodes and due to oxygen drift ($V_{O_2,acc}(t_1 \rightarrow t_2)$). $\varphi(t_2)$ may be again calculated from the oxygen peak area of the gas chromatogram. Now, $V_{GC}(t_2)$ would be composed of the terms:

$$V_{GC}(t_2) = V_{O_2}(t_0) - 2\ \text{mL}\ \varphi(t_0) + V_{O_2,acc}(t_0 \rightarrow t_1) - 2\ \text{mL}\ \varphi(t_1) + V_{O_2,acc}(t_1 \rightarrow t_2) \quad \textbf{(14)}$$

Therefore, $V_{O_2}(t_2)$ has to be calculated from $V_{GC}(t_2)$ by correcting it for sampling during t_0 and t_1:

$$V_{O_2}(t_2) = V_{GC}(t_2) + 2\ \text{mL}\ \varphi(t_0) + 2\ \text{mL}\ \varphi(t_1) \quad \textbf{(15)}$$

The previous derivation may be verified by inserting **(14)** for $V_{GC}(t_2)$ in **(15)**:

$$V_{O_2}(t_2) = V_{O_2}(t_0) - 2\ \text{mL}\ \varphi(t_0) + V_{O_2,acc}(t_0 \rightarrow t_1) - 2\ \text{mL}\ \varphi(t_1) + V_{O_2,acc}(t_1 \rightarrow t_2) \quad \textbf{(16)}$$

$$+ 2\ \text{mL}\ \varphi(t_0) + 2\ \text{mL}\ \varphi(t_1) = V_{O_2}(t_0) + V_{O_2,acc}(t_0 \rightarrow t_1) + V_{O_2,acc}(t_1 \rightarrow t_2)$$

For n measurements, the general form of equation **(6)** is obtained:

$$V_{O_2}(t_n) = V_{GC}(t_n) + 2\ \text{mL} \sum_{k=0}^{n-1} \varphi(t_k)\ ,\ \text{with}\ n > 0 \quad \textbf{(6)}$$

As an example, for measurement number 6 at t_5, $\varphi(t_n)$ has to be summarized from k = 0 until n - 1 = 4.

5.2. Wavelength-dependent Sensitivity of the Si calibration Cell used for EQE Measurements

Table 3: S_{Si} values of the Si calibration cell used for EQE measurements.

λ / nm	S_{Si} / A W^{-1}	λ / nm	S_{Si} / A W^{-1}	λ / nm	S_{Si} / A W^{-1}
350	0.153	420	0.205	490	0.252
360	0.155	430	0.2125	500	0.259
370	0.155	440	0.22	510	0.2655
380	0.165	450	0.2265	520	0.272
390	0.178	460	0.233	530	0.2775
400	0.188	470	0.239	540	0.283
410	0.1965	480	0.245	550	0.288

6. References

[1] L. Maugeri, *The age of oil: The mythology, history, and future of the world's most controversial resource*, 1st ed., Praeger, Westport, Conneticut **2007**.

[2] W. D. Devine, *J. Eco. History* **1983**, *43* (2), 347 – 372.

[3] British Petroleum BP p.l.c., *bp Statistical Review of World Energy 2021*, 70th ed., London **2021**.

[4] M. Zielińsk, J. Fletcher, M. Ewen, N. Fulghum, P. Tunbridge, D. Jones, A. Lolla, A. Candlin, B. Worthington, C. Moore, H. Broadbent, *Global Electricity Review 2022*, 3rd ed., London **2022**.

[5] Organization of the Petroleum Exporting Countries, OPEC, *2021 World Oil Outlook: 2045*, 15th ed., Wien **2021**.

[6] N. Abas, A. Kalair, N. Khan, *Futures* **2015**, *69* 31 – 49.

[7] N. Armaroli, V. Balzani, *Chem. Eur. J.* **2016**, *22* (1), 32 – 57.

[8] A. Harriman, *Phil. Trans. R. Soc. A.* **2013**, *371* (1996), 20110415.

[9] P. Migowski, A. F. Feil, *Recycl. Catal.* **2016**, *3* (1), 1 – 12.

[10] Z. Wang, Y. Gu, L. Wang, *Front. Energy* **2021**, *15* (3), 596 – 599.
[11] M. S. Prévot, K. Sivula, *J. Phys. Chem. C* **2013**, *117* (35), 17879 – 17893.
[12] T. A. Kistler, N. Danilovic, P. Agbo, *J. Electrochem. Soc.* **2019**, *166* (13), H656-H661.
[13] V. Andrei, R. L. Z. Hoye, M. Crespo-Quesada, M. Bajada, S. Ahmad, M. de Volder, R. Friend, E. Reisner, *Adv. Energy Mater.* **2018**, *8* (25), 1801403.
[14] S. Ho-Kimura, W. Soontornchaiyakul, Y. Yamaguchi, A. Kudo, *Catalysts* **2021**, *11* (1), 136.
[15] A. Kudo, Y. Miseki, *Chemical Society reviews* **2009**, *38* (1), 253 – 278.
[16] G. Talasila, S. Sachdev, U. Srivastva, D. Saxena, S. Ramakumar, *Energy Reports* **2020**, *6* 1963 – 1972.
[17] A. J. Bard, L. R. Faulkner, *Electrochemical Methods: Fundamentals and Applications*, 2nd ed., John Wiley & Sons, Inc., New York **2001**.
[18] K. Rajeshwar, *Semiconductor Electrodes and Photoelectrochemistry: Chapter 1 - Fundamentals of Semiconductor Electrochemistry and Photoelectrochemistry*, 1st ed., Encyclopedia of Electrochemistry, Vol. 6 (Eds: A. J. Bard, M. Stratmann), Wiley-VCH Verlag GmbH, Weinheim **2002**.
[19] C. H. Hamann, W. Vielstich, *Elektrochemie: Kapitel 11.2 - Photoelektrochemie*, Wiley-VCH Verlag GmbH, Weinheim **1998**.
[20] A. J. Bard, *Science* **1980**, *207* (4427), 139 – 144.
[21] P. Arunachalam, A. M. Al Mayouf, *Noble Metal-Metal Oxide Hybrid Nanoparticles - Fundamentals and Applications: Chapter 28: Photoelectrochemical Water Splitting*, In: Micro and Nano Technologies (Eds: S. Mohapatra, T. A. Nguyen, P. Nguyen-Tri), Woodhead Publishing, Sawston **2019**.
[22] K. J. McDonald, K.-S. Choi, *Energy Environ. Sci.* **2012**, *5* (9), 8553.
[23] R. J. Meyer, *Gmelins Handbuch der anorganischen Chemie: Wismut und radioaktive Isotope*, 8th ed., Verlag Chemie G.m.b.H., Berlin **1927**.
[24] C. Gabrielli, P. Moçotéguy, H. Perrot, D. Nieto-Sanz, A. Zdunek, *Electrochimica Acta* **2006**, *51* ((8-9)), 1462 – 1472.
[25] L. Jing, Y. Qi-Hua, Z. Zhao, *Trans. Nonferrous Met. Soc. China* **2010**, *20* (1), 97 – 101.
[26] T. Oekermann, *On Solar Hydrogen and Nanotechnology: Chapter 11.6: Use of Additives in ZnO Electrodeposition*, 1st ed. (Eds: L. Vayssieres), John Wiley & Sons (Asia) Pte Ltd, Singapur **2010**.
[27] T. Yoshida, D. Komatsu, N. Shimokawa, H. Minoura, *Thin Solid Films* **2004**, *451-452* 166 – 169.
[28] Y. Kuang, Q. Jia, H. Nishiyama, T. Yamada, A. Kudo, K. Domen, *Adv. Energy Mater.* **2016**, *6* (2), 1501645.
[29] J. W. Verhoeven, *Pure and Applied Chemistry* **1996**, *68* (12), 2223 – 2286.
[30] T. W. Kim, K.-S. Choi, *Science (New York, N.Y.)* **2014**, *343* (6174), 990 – 994.
[31] Z. Chen, H. N. Dinh, E. Miller, *Photoelectrochemical Water Splitting - Standards, Experimental Methods and Protocols: Chapter 5: UV-Vis Spectroscopy*, 1st ed., Springer, New York **2013**.
[32] M. Irimia-Vladu, E. D. Głowacki, P. A. Troshin, G. Schwabegger, L. Leonat, D. K. Susarova, O. Krystal, M. Ullah, Y. Kanbur, M. A. Bodea, V. F. Razumov, H. Sitter, S. Bauer, N. S. Sariciftci, *Adv. Mater.* **2012**, *24* (3), 375 – 380.
[33] W. M. Haynes, *CRC Handbook of Chemistry and Physics: Section 3: Physical Constants of Organic Compounds: Indigo - Compound 6239*, 97th ed., CRC Press, Boca Raton **2017**.
[34] P. Pookmanee, S. Kojinok, R. Puntharod, S. Sangsrichan, S. Phanichphant, *Ferroelectrics* **2013**, *456* (1), 45 – 54.
[35] K. Tolod, S. Hernández, N. Russo, *Catalysts* **2017**, *7* (12), 13.

[36] G. Kaur, O. P. Pandey, K. Singh, *Phys. Status Solidi A* **2012**, *209* (7), 1231 – 1238.
[37] T. Tran-Phu, H. Chen, R. Bo, I. Di Bernardo, Z. Fusco, A. N. Simonov, A. Tricoli, *Energy Technol.* **2019**, *7* (8), 1801052.

List of Abbreviations

Abs	Absorbance	HER	Hydrogen evolution reaction
Ag|AgCl|3 M KCl	Silver-silver chloride-3 M potassium chloride	HNO_3	Nitric acid
ATR	Attenuated total reflectance	I^-	Iodide ion
$Bi(NO_3)_3 \cdot 5\ H_2O$	Bismuth(III) nitrate pentahydrate	NaI	Sodium iodide
Bi_2O_3	Bismuth(III) oxide	NaOH	Sodium hydroxide
Bi^{3+}	Bismuth(III) ion	OER	Oxygen evolution reaction
$[BiI_4]^-$	Tetratiodo bismuthate	PEC	Photoelectrochemical
BiOI	Bismuth oxyiodide	Pt	Platinum
$BiONO_3 \cdot H_2O$	Bismuth subnitrate	PV	Photovoltaic
BiOOH	Bismuth oxyhydroxide	PV-EC	Phototvoltaic-electrochemical
$BiVO_4$	Bismuth vanadate	RE	Bismuth vanadate
CE	Counter electrode	SEM	Scanning electron microscopy
CV	Cyclic voltammetry	Si	Silicon
DMSO	Dimethyl sulfoxide	*T*	Transmittance
E_g	Bandgap energy	V_2O_5	Vanadium pentoxide
EQE	External Quantum Efficiency	$VO(acac)_2$	Vanadyl acetylacetonate
FTIR (spectroscopy)	Fourier-transform infrared (spectroscopy)	vs. NHE	Versus normal hydrogen electrode
FTO	Fluorine-doped tin oxide	WE	Working electrode
GC	Gas chromatography	Xe	Xenon

List of Figures

List of Tables